physica status solidi a
www.pss-a.com

Atom Probe Tomography Advances Chalcogenide Phase-Change and Thermoelectric Materials

Yuan Yu, Oana Cojocaru-Mirédin,* and Matthias Wuttig**

Main-group chalcogenides show outstanding performance for phase-change data storage and thermoelectric energy conversion applications. A common denominator for these different property requirements is ascribed to the metavalent bonding (MVB) mechanism. Atom probe tomography (APT) provides a unique way to distinguish MVB from other bonding mechanisms by determining the bond-breaking behavior. Specifically, an unusually high probability to dislodge several fragments upon one successful laser pulse (probability of multiple events [PME]) is found in metavalently bonded crystalline phase-change and thermoelectric materials. In contrast, amorphous phase-change materials and poor thermoelectrics usually show lower PME values. This indicates that the large optical and electrical contrast between the crystalline and amorphous chalcogenides is attributed to a transition of chemical bonding. A strong correlation between high thermoelectric performance and large PME is also established. Besides, APT can investigate structural defects on the subnanometer scale. These characteristics reveal the interdiffusion of elements in interfacial phase-change materials and revisit its switching mechanism. The complex role of structural defects such as grain boundaries in tuning the thermoelectric properties can also be unraveled by investigating the local composition and bonding mechanism at defects. This review demonstrates that APT is a powerful technique for designing phase-change and thermoelectric materials.

1. Introduction

Main-group chalcogenides are widely used for phase-change data storage[1–3] and thermoelectric energy conversion.[4–6] Phase-change materials (PCMs) can be switched reversibly between the amorphous and crystalline states, which are equivalent to the binary numbers "0" and "1", respectively.[1,7] Superior PCMs require an unconventional combination of properties including high-speed phase transitions, and large optical and resistance contrast between the two states for rewriteable optical and nonvolatile electronic data storage, respectively.[1,8] On the other hand, thermoelectric materials require a large electrical conductivity (σ) as in metals, a high Seebeck coefficient (S) as in semiconductors, and a low thermal conductivity (κ) as in amorphous materials, to enable a high thermal-to-electricity conversion efficiency, summarized in the dimensionless figure-of-merit $zT = S^2\sigma T/\kappa$.[9–11] Interestingly, these demanding and seemingly contradictory requirements are found in a class of chalcogenide compounds such as GeTe and Sb_2Te_3, as well as their alloys.[3,12,13] This surprising property combination has motivated us to investigate the underlying mechanisms responsible for the unique portfolio of properties.

The properties of materials are often governed by two types of factors. One of them is related to intrinsic properties controlled by the way the constituent elements are connected, i.e., by chemical bonding mechanisms.[14] The other factor is related to extrinsic properties controlled by structural defects such as vacancies,[15,16] dislocations,[17–19] grain boundaries (GBs),[20–23] or precipitates.[24–26] Crystalline main-group chalcogenides show unique intrinsic properties, e.g., a high optical dielectric constant ($\varepsilon_\infty > 15$), a large Born effective charge (Z^*, between 4 and 6), a high coordination number that violates the "8-N" rule, and a strong lattice anharmonicity of transverse optical modes ($\gamma_{TO} > 3$).[27] These properties are fingerprints of an unconventional chemical bonding mechanism, termed metavalent bonding (MVB).[27–29] MVB is formed by the bonding of p-state valence electrons between adjacent atoms with on average one electron per bond (half of an electron pair), i.e., with a two-center one-electron (2c–1e) configuration.[30] This is different from the classic definition of covalent bonding by Lewis,[31] characterized by an electron pair between two atoms, i.e., 2c–2e. MVB is also different from hypervalent bonding in which a configuration of 3c–4e

Y. Yu, O. Cojocaru-Mirédin, M. Wuttig
Institute of Physics (IA)
RWTH Aachen University
52056 Aachen, Germany
E-mail: yu@physik.rwth-aachen.de; wuttig@physik.rwth-aachen.de

O. Cojocaru-Mirédin
Department of Sustainable Systems Engineering (INATECH)
Albert-Ludwigs-Universität Freiburg
79110 Freiburg, Germany
E-mail: oana.cojocaru-miredin@mail.inatech.uni-freiburg.de

M. Wuttig
Peter Grünberg Institute (PGI 10)
Forschungszentrum Jülich
52428 Jülich, Germany

The ORCID identification number(s) for the author(s) of this article can be found under https://doi.org/10.1002/pssa.202300425.

DOI: 10.1002/pssa.202300425

is utilized, which is electron-rich, while metavalent bonds are electron-deficient.[30,32] In contrast, the amorphous state of these materials does not employ MVB due to structural distortions. Instead, covalent bonding prevails in the amorphous phase, which leads to a much weaker optical reflectance and a larger electrical resistivity.[33,34] This chemical bonding transition between metavalent and covalent bonding generates a large optical or electrical contrast between the two states, essential for data storage.[14,35–37] The view that metavalent bonding leads to unique material properties is also supported by a data-driven classification algorithm. Employing seven different material properties including several discussed above (Z^*, ECoN, σ) and additional properties such as the bandgap, as well as the atomic and mass density, plus the melting temperature lead to a classification into four different types of solids governed by metallic, ionic, covalent, and metavalent bonding.[38]

This MVB mechanism also explains the intrinsically high thermoelectric performance of many chalcogenides.[11,29,39,40] The half-filled *p*-band should lead to a metallic ground state. Yet, this configuration is unstable against either a small structural distortion (also called Peierls distortion) or a moderate charge transfer.[37,41,42] Both processes open the bandgap, turning these chalcogenides into narrow-gap semiconductors. Thus, these MVB chalcogenides are also called incipient metals.[27] As a result, they show a relatively high electrical conductivity close to the Mooij value for bad metals[43,44] as well as large Seebeck coefficients for semiconductors.[45] In addition, the soft chemical bonds and large anharmonicity lead to low thermal conductivity.[46–48] All these factors are beneficial for high thermoelectric performance. Typical MVB thermoelectrics such as GeTe,[49] PbTe,[50] and Bi_2Te_3[51] show intrinsic zT values close to 1. Their zT values can be further improved to over 2 by introducing extrinsic lattice defects such as dopants, dislocations, and interfaces.[52–56] In this regard, the distribution of dopants, the number density and composition of dislocations, and the phase structure of GBs all impact the electron and phonon transport properties.

Studying the chemical bonding mechanisms and the lattice defects of these chalcogenides is thus critical for designing desired phase-change and thermoelectric properties without time-consuming "trial and error" processes. Besides the MVB indicators summarized above,[27] this bonding mechanism also exhibits an abnormal bond rupture in laser-assisted atom probe tomography (APT) as compared to classic metallic, ionic, and covalent bonding mechanisms.[43,57] **Figure 1**a sketches the working principle of APT,[58,59] which relies on the principle of field-induced ionization and evaporation. A direct-current voltage is applied to a needle-shaped specimen with an apex radius of about 50–100 nm, to generate an extremely high electric field on the order of tens of volts per nanometer. The surface atoms are preferentially positively ionized under such a high electric field and experience a large electric field force toward the detector. The evaporation process is triggered by applying either a negative voltage pulse to the local electrode or a picosecond laser pulse to the specimen.[59] This pulse signal also initiates the starting time of the evaporation, while the ending time will be recorded by the microchannel plate when the ion arrives. Thus, the time-of-flight of the ion can be calculated, which gives the chemical identity (mass-to-charge ratio) of the detected ion. The interaction of the ion and the microchannel plate converts a single ion impact into a shower of electrons and amplifies the electronic

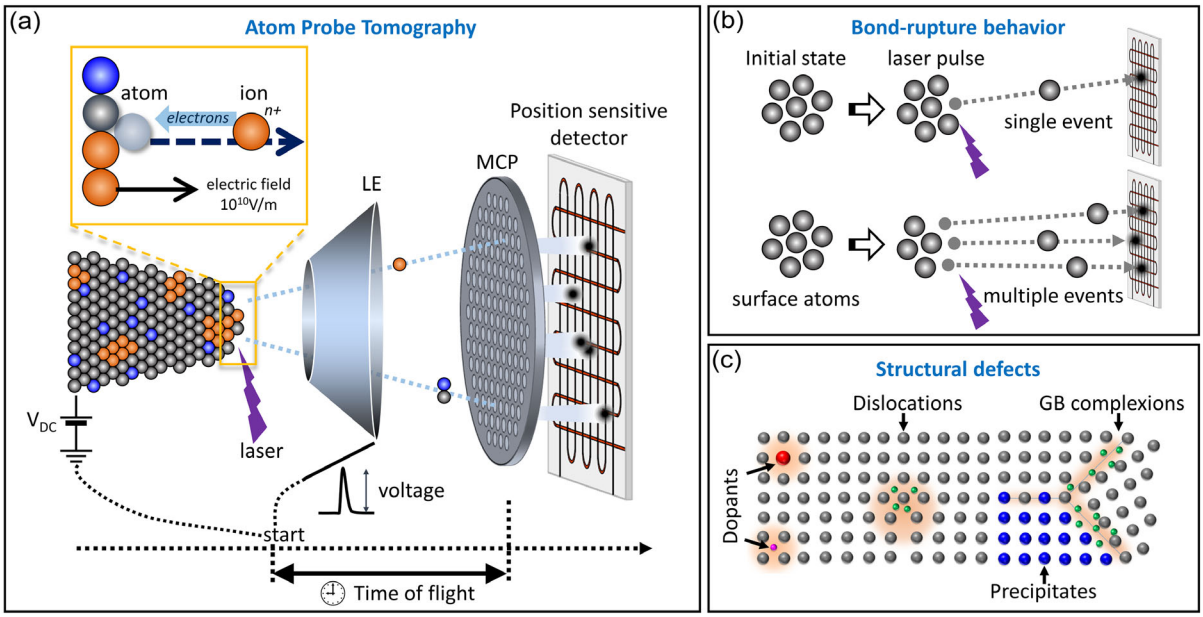

Figure 1. Schematic of APT and its unique potential to characterize the chemical bond-rupture behavior and structural defects. a) Sketch showing the working principle and main components of APT. b) Definition of a single event (upper) and multiple events (lower) in APT measurements. The process which generates one single ion with one successful laser pulse is called a single event, while multiple ions are dislodged with one laser pulse refers to multiple events. The ratio of the multiple events to the total events is called the probability of multiple events, abbreviated as PME. c) APT can reveal the chemical composition and 3D morphology of structural defects including dopants, dislocations, GB complexions, and precipitates.

signal for precise detection of the x- and y-coordinates.[60] The z-coordinate is derived from the ion impact sequence. As a consequence, the 3D coordinates and chemical identity of each detected ion can be obtained, generating a 3D map of constituent elements with a spatial resolution down to the subnanometer scale and a chemical sensitivity in the range of tens of parts per million.[61,62] Note that the desorption of atoms from the specimen surface is accompanied by the breaking of chemical bonds. This process induces a peculiar phenomenon for metavalent materials. For a well-controlled APT experiment with a small detection rate, i.e., only a small fraction of laser pulses breaks the bond, one successful laser pulse often dislodges only one single ion, which is called a single event, as illustrated in Figure 1b. Once more than one ion is removed from the surface under a laser pulse, several ions will be detected and the corresponding process is called multiple events (Figure 1b).[63] Extensive studies have demonstrated that the probability of multiple events (PME) for MVB materials is much higher than that for any other compounds employing covalent, ionic, and metallic bonding.[11,43,57,64–66] Therefore, a high PME value (>60%) serves as a very plausible indicator of MVB. Additionally, the high spatial and chemical resolution of APT enables characterizing structural defects,[67–70] which are important for tuning thermoelectric properties,[21–24,71–77] as summarized in Figure 1c.

In this review, we will summarize the application potential of APT in PCMs and thermoelectric materials. We start by introducing the relationships between chemical bonding mechanisms and the bond-rupture behavior. Subsequently, typical results will be illustrated, showing how APT helps to understand PCMs. After that, several examples of thermoelectric materials will be presented, demonstrating how the chemical bonding mechanisms and lattice defects can be utilized to design thermoelectrics with the critical information provided by APT. Finally, the combination of APT with other techniques in further promoting the understanding of bonding–structure–property relationships is discussed.

2. Unconventional Bonding Mechanism and Abnormal Bond-Rupture Behavior

Chemical bonds form by the Coulomb attraction or repulsion between atoms resulting from different behaviors of valence electrons such as electron transfer or electron pair formation. Yet, there are gradual transitions between these two. Thus, it seems that there is no clear demarcation line between them. Yet, from the perspective of various properties of condensed matter, it is still very useful to define different types of chemical bonds. The valence electrons of neighboring atoms can interact with each other either through sharing of electrons (electron-pair formation) as in covalent and metallic bonds or through the transfer of electrons as in ionic bonds.[78] In this vein, the number of electrons shared (ES) and electrons transferred (ET) can be regarded as natural chemical bonding descriptors. With the emergence and development of quantum-chemical calculation tools,[79,80] these two values can be quantitatively determined. Accordingly, a chemical bonding map using ES and ET as coordinates can be plotted, as shown in **Figure 2**a.[28,81] Covalent bonding can be found in the upper-left region of the map due to the formation of an electron pair. In contrast, ionic bonding is located at the bottom-right corner due to the large electron transfer between adjacent atoms. All ionic compounds show some degree of covalent bonding upon limited electron sharing. This is also demonstrated by the ES–ET map, which shows that many of the ionic and covalent compounds locate around the connecting line between perfect covalent (ES = 2, ET = 0) and perfect ionic (ES = 0, ET = 1) solids. Elemental metals and van der Waals materials prevail at the bottom-left corner due to the absence of electron transfer and a small value of electrons shared. Interestingly, the crystalline main-group chalcogenides that show excellent phase-change memory and thermoelectric performance cannot be assigned to any of these bonding mechanisms on the map. Instead, they show an ES value near one (half of an electron pair) due to the half-filled bond and a moderate ET value. This bonding region has been denoted as metavalent bonding. This name has two meanings,

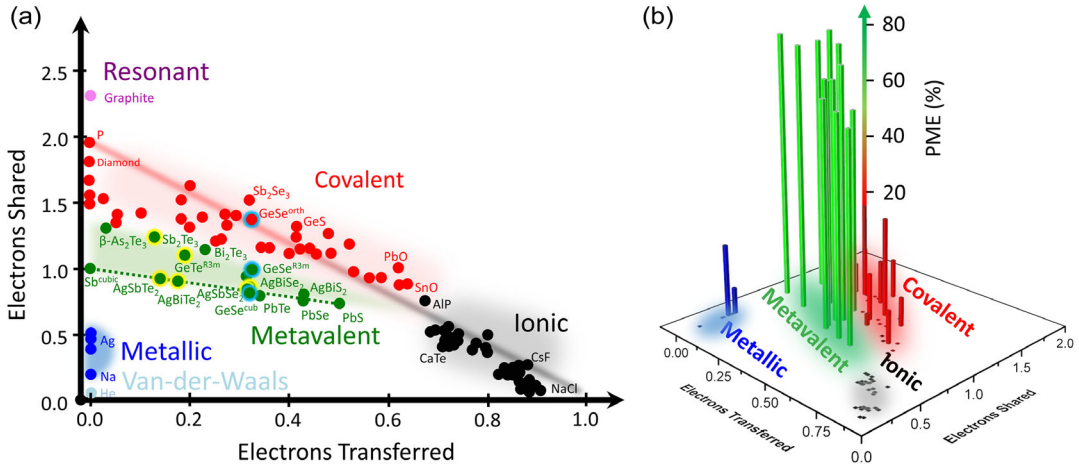

Figure 2. Relationship between chemical bonding mechanisms and the bond-breaking behavior in APT measurements. a) Demarcation of different chemical bonding mechanisms by a quantum-chemical map spanned by the numbers of ES and ET normalized to the formal oxidation state of compounds. b) PME values plotted as the third axis on the ES-ET basal plane, showing the unconventional bond-breaking process of metavalent bonding with PME typically larger than 60%. Reproduced with permission.[81] Copyright 2023, WILEY-VCH.

the Greek prefix "meta" stands for "beyond", expressing that metavalent bonding is beyond ordinary covalent bonding. Yet, metavalent bonding also stands for a bonding mechanism between metallic and covalent bonding, nevertheless, with distinctively different properties. These different bonding mechanisms are not classified based only on the values of ES and ET, especially at the borders. The different colors that represent different bonding mechanisms are defined in combination with characteristic property values determined for the dielectric function and the Born effective charge,[27] as well as the abnormal bond-rupture behavior.[57] These properties are classified into different groups using the expectation maximization (EM) algorithm without any human interference, which is in excellent agreement with different bonding mechanisms devised by material scientists.[38] The MVB origin of these special structural, electrical, and optical properties has been summarized in several papers.[14,29,30,44] In this article, we focus on the unique bond-breaking phenomenon observed in APT measurements for MVB compounds. In turn, APT provides a straightforward way to distinguish metavalent bonding.

As has been briefly explained in Figure 1a, the working principle of APT enables its unparalleled capability of determining bond-breaking behavior. Figure 2b plots the PME values for various compounds utilizing different bonding mechanisms on the basal plane of Figure 2a.[11,57,81] The difference between the MVB region (green) and others is striking. All the MVB compounds show a PME value greater than 60%, while others often show a much smaller PME value. Note that these different PME values are not caused by the changes in composition or structure but by the bonding mechanism. For example, amorphous chalcogenides show low PME values due to their covalent bonding nature, while their crystalline counterpart with the same composition shows much higher PME values due to MVB.[57] Nevertheless, it is important to note that the PME value slightly changes with a standard deviation of about 10% within a large range of measurement parameters of APT.[57] Yet, this variation is much smaller than the change of PME upon going from metavalent to covalent bonding. We should also keep in mind that the low PME value could also be induced by the Ga beam contamination and damage to the sample, which can be minimized with careful sample preparation using a focused ion beam.[82] Therefore, there is a clear correlation between MVB and high PME in APT measurement. The potential causality between MVB and high PME could be related to the nature of weak bonds and the long-range interaction between *p*-orbital electrons for MVB. More rigorous studies taking the laser–matter interactions,[83] the effective mass of charge carriers,[84] and the band bending under high fields[84] into account are encouraged. The results are expected to reveal the chemical bonding origin of high PME.

3. Applications of APT to PCMs

PCMs can be used for data-storage applications.[1] They are considered one of the most promising candidates for achieving storage-class nonvolatile memory and neuro-inspired computing with low power consumption.[85] PCMs can realize the fast and reversible phase transition between amorphous and crystalline states induced by a nanosecond laser or voltage pulse. The amorphous state shows a low optical reflectance and a high electrical resistivity, which corresponds to the "zero" binary bit. In contrast, the crystalline state shows a much larger optical reflection and electrical conductivity, corresponding to the "one" binary bit. Therefore, rewriteable optical or nonvolatile electronic data storage can be achieved by assigning binary information to these two states.[1,7,8,85–87] As the crystallization of amorphous regions is accompanied by a change of bonding mechanisms, it seems obvious that a solid understanding of the chemical bonding mechanism in both states can greatly improve our potential to design PCMs.

Superior PCMs have been found along the tie line between GeTe and Sb_2Te_3, which all utilize octahedral-like coordination in their crystalline state.[3] However, the average number of valence *p*-electrons for bonding per atom is only three, if we consider Sb_2Te_3 to have a vacancy layer between adjacent Te planes. This means that only one electron is shared between two neighboring atoms forming the bond. Such a special chemical bonding mechanism is called metavalent bonding,[27,30] as we have elaborated above. MVB requires the second and higher neighbors to be aligned,[34] which cannot be fulfilled in the amorphous structure due to the absence of medium- and long-range ordering. Thus, the chemical bonding mechanism in the amorphous state must be different from its crystalline counterpart. Zhu et al.[57] studied the bond-breaking behavior of prototypical PCMs such as $Ge_2Sb_2Te_5$ in both amorphous and crystalline states. The amorphous PCMs show a relatively small PME value. In stark contrast, their crystalline phases without changing composition show a much larger PME value, as shown in **Figure 3**a. Such a strong contrast in PME is accompanied by an abrupt change in the optical dielectric constant, which is critical for optical data storage. Figure 3a contains fewer data points than that in Figure 2a. The properties of metastable compounds can be calculated, even though it might be impossible to produce the corresponding material. An example is cubic, rocksalt-structured GeTe, which cannot be stabilized under atmospheric conditions (1 atm, room temperature). Hence, we cannot study this material by APT, yet we can study it in quantum chemical calculations. MVB in the crystalline phase ensures that a pronounced property contrast between the crystalline and the amorphous phase exists. It does not ensure however that the amorphous phase will also be stable at room temperature. This can be seen for Sb as well as SnTe. Sb crystallizes rapidly at room temperature and only in the form of very thin films can it be stabilized enough to avoid crystallization. SnTe is another example of a material, which employs MVB in the crystalline state, yet cannot be easily stabilized in the glassy state due to very fast recrystallization at room temperature. Finally, materials such as Sb_2Se_3 and Sb_2S_3 do not employ MVB in the crystalline state, which can be found at the bottom-left in Figure 3a, yet are interesting for data storage. In these materials, the density contrast between the amorphous and the crystalline state is sufficient to create moderate changes in optical properties. Nevertheless, these considerable variations in PME and dielectric constant have not been found in non-PCMs, such as GeSe and Si, between their amorphous and crystalline states. In this regard, APT provides a unique way to identify the unconventional bonding mechanism for PCMs. It also helps us to better understand the phase-change

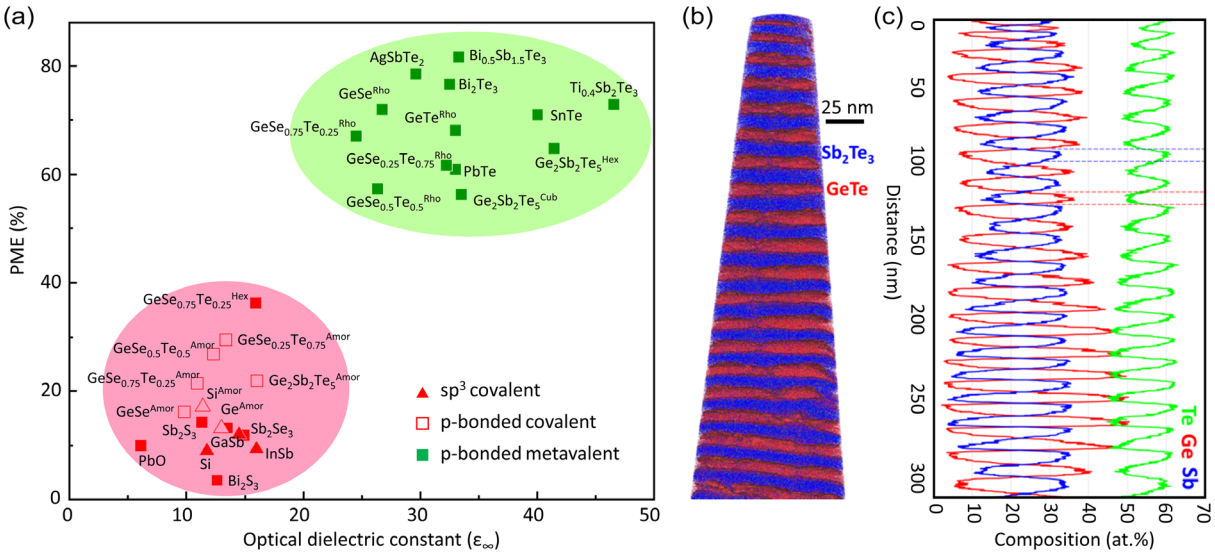

Figure 3. Applications of APT to PCMs. a) PME values of different compounds utilizing different bonding mechanisms. A high PME value is only found for crystalline *p*-bonded metavalent solids, while their amorphous counterparts show a low PME value. b) Reconstructed 3D map of GeTe–Sb_2Te_3 superlattices showing the alternative stacking and element distribution in each layer. c) 1D composition profile across several interlayers demonstrating the intermixing between adjacent layers. Inset (a): Reproduced with permission.[57] Copyright 2018, WILEY-VCH. Insets (b) and (c): Reproduced with permission.[92] Copyright 2019, IOP Publishing.

mechanism, which is indeed induced by a chemical bonding transition. This bonding transition can be controlled by systematically changing the values of ES and ET via tuning the stoichiometry.[37] As a result, the crystallization and vitrification kinetics,[88] in addition to the large property contrast, can be manipulated. In this regard, some MVB compounds that show poor phase-change properties, such as PbS and As_2Te_3, could also be tuned into good PCMs through alloying, for example, the alloy between As_2Te_3 and Sb_2Te_3.[89] Beyond the average number of PME as illustrated in Figure 3a, the 3D APT data can also provide a spatially resolved PME map that could identify the crystallized regions within an amorphous matrix and vice versa, which probes the different states for SET and RESET in a switching cell.[57]

Besides the traditional PCMs, the so-called interfacial PCMs (i-PCMs) have attracted much attention due to their fast switching speed and low energy consumption.[90] It has been proposed that the i-PCM switching mechanism depends on the local atomic flipping of Ge atoms at the interface between GeTe and Sb_2Te_3, while the interlayer diffusion is negligible in the i-PCM structure. Yet, this explanation is still under debate because the superlattice structure could also enhance the process similar to bulk PCM devices.[91] Owing to the high spatial and chemical resolution of the APT technique, the intermixing between GeTe and Sb_2Te_3 layers has been unambiguously revealed.[92] Figure 3b shows the alternative stacking layers of GeTe and Sb_2Te_3 displayed in red and blue, respectively. Interestingly, a close examination of the composition profile across multiple layers indicates the interdiffusion between Ge and Sb. The concentration of Ge in the Sb_2Te_3 layers varies between 4 and 7 at% and the content of Sb changes from 5 at% to 13 at% in the GeTe layers. This contradicts the i-PCM switching mechanism proposed originally[90] but is in line with the viewpoint that intermixing is necessary for epitaxial growth.[93] Moreover, APT studies also revealed the preferential formation of a $Ge_2Sb_2Te_5$ phase at high-angle GBs and $Ge_1Sb_2Te_4$ at low-angle GBs,[92] which are typical PCMs but not i-PCMs.

4. Applications of APT to Thermoelectric Materials

Similar to the case of understanding PCMs, APT also provides a facile way to identify high-performance thermoelectric materials because MVB leads to both high thermoelectric properties and large PME values.[11,57] For example, even though GeSe is a close counterpart to PbTe and GeTe, their thermoelectric properties are significantly different. While GeSe shows a maximum zT value below 0.1,[94] PbTe and GeTe can reach zT as high as above 2.[95,96] **Figure 4**a shows that the PME value of pristine GeSe is about 30%,[81] corroborating its iono-covalent bonding nature as indicated in Figure 2a.[42] Extensive studies have demonstrated that the zT value of GeSe can only be enhanced by alloying with compounds such as GeTe,[97] Sb_2Te_3,[98] $AgSbSe_2$,[99] $AgSbTe_2$,[100] $AgBiSe_2$,[101] and $AgBiTe_2$.[39] Note that some other compounds such as InTe[64,102] and $MnCdTe_2$,[103] which have also been reported effective in improving the zT of GeSe, include a large content of Te, resembling the effect of alloying GeTe. Interestingly, all these compounds are located in the MVB region as highlighted by yellow circles in Figure 2a. This is not a coincidence but instead, a strong causality exists. APT experiments show a high PME value (>70%) in the GeSe–15%$AgSbSe_2$ alloy in Figure 4a.[81] This indicates the establishment of MVB in the new GeSe alloy. Consequently, the zT value is improved by a factor of more than 10 from pristine covalent GeSe to the MVB GeSe–15%$AgSbSe_2$ alloy (Figure 4b). The MVB origin of high thermoelectric performance has been thoroughly explained in previous work.[11,64,81] Here, we demonstrate that APT provides a facile approach to screen potential high-performance

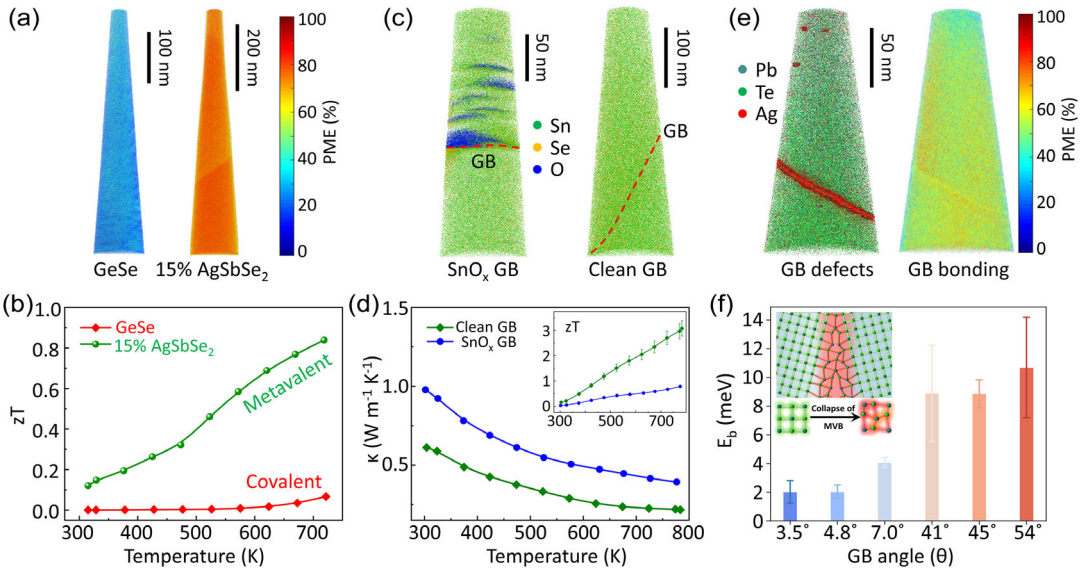

Figure 4. Applications of APT to thermoelectric materials. a) Design of thermoelectrics by enabling the bonding transition from covalent GeSe to metavalent GeSe–15%$AgSbSe_2$ alloy. The corresponding bonding mechanisms of the two phases are revealed by 3D PME maps characterized by APT. b) The thermoelectric figure-of-merit zT is greatly improved in the metavalently bonded phase as compared to the covalently bonded phase. c) Impact of defect chemistry on thermoelectric properties. APT reveals the existence and removal of SnO_x at GBs in SnSe. d) Temperature-dependent thermal conductivity of samples with clean GBs and SnO_x at GBs. Inset shows the corresponding zT values of these two samples. e) Segregation of Ag dopants to the GB in PbTe and the associated 3D PME map, showing the local composition and bonding mechanism at the GB, respectively. f) Potential barrier height (E_b) for charge carrier scattering at GBs as a function of the GB misorientation angle. Inset illustrates the collapse of metavalent bonding at the high-angle GB, contributing to the increased GB barrier height. Insets (a) and (b): Reproduced with permission.[81] Copyright 2023, WILEY-VCH. Insets (c) and (d): Reproduced with permission.[109] Copyright 2021, Springer Nature. Insets (e) and (f): Reproduced with permission.[116] Copyright 2023, Springer Nature.

thermoelectrics given the strong correlations between high PME and high thermoelectric performance enabled by MVB.

Thermoelectric semiconductors often contain a certain amount of impurities, which can greatly influence the performance of materials.[4–6,71,104] A representative example can be found in SnSe. This compound has attracted intensive research interests in thermoelectrics since its high zT value of 2.6 was reported in 2014.[105] The ultralow thermal conductivity in single-crystal SnSe was considered the leading cause of the high zT value. Yet, the corresponding polycrystalline SnSe counterpart prepared by conventional methods often shows unexpectedly higher thermal conductivity and lower zT value,[106] although GBs are usually considered phonon scatterers. This abnormal phenomenon has puzzled the thermoelectric community for years. Even though the formation of tin oxides has been assumed the potential culprit for the degraded performance,[107,108] direct and convincing evidence was provided only recently with the involvement of APT.[109] The left figure of Figure 4c shows the distribution of elements in as-synthesized polycrystalline SnSe by conventional processes. Besides Sn and Se atoms, many O atoms are also observed at and around the GB even though the raw elements are of high purity. Enlightened by this information, Zhou et al.[109] purified the raw elements and as-synthesized powders to remove the residual oxygen as much as possible. Finally, a clean GB without tin oxides is obtained as proved by APT measurements (Figure 4c, right). Due to the removal of thermally conductive SnO_x, the lattice thermal conductivity is greatly reduced and the zT value is significantly increased in the purified polycrystalline SnSe sample, even greater than that in the single-crystal form.

The impurities at GBs influence not only the phonon transport but also the electrical properties. Several thermoelectric compounds such as Mg_3Sb_2,[110,111] half-Heusler alloys,[112] and elemental Te[113] show prominent charge carrier scattering at GBs. The phenomenon of thermally activated electrical conductivity can be gradually inhibited by increasing the grain size.[110] APT measurements show Mg deficiency at GBs of Mg_3Sb_2, explaining the formation of a potential barrier to scatter electrons.[114] Yet, this is not direct evidence of the charge scattering at GBs because the modification of GB density by annealing is also accompanied by the change of properties of the grain interior.[115] To circumvent this issue, Wu et al.[116] designed a novel method to measure the charge carrier transport across an individual GB and then correlated the electrical properties with local microstructures. They systematically compared the transport behavior across various GBs with different misorientation angles in Ag-doped PbTe. According to the trapping state model,[117,118] the carrier scattering at GBs is evaluated by the potential barrier height, which depends on the density of the trapping states and the static dielectric constant.[117] The APT technique makes it possible to experimentally estimate these two parameters by revealing the GB chemical composition and bonding mechanism. Figure 4e (left) shows the enrichment of Ag dopants at a high-angle GB spreading over the whole GB plane. In contrast, the segregation of dopants at low-angle GBs (not shown here) is only observed at the dislocation cores.[116] The Gibbsian

interfacial excess analysis indicates that the density of trapping states at the high-angle GB is about 1.5 times larger than that at the low-angle GB, partly leading to the larger GB barrier height, as shown in Figure 4f. Due to the unique capability of APT in identifying MVB as explained above, the PME map can further discern MVB and non-MVB regions in property space. Figure 4e (right) shows the PME map of the corresponding region probed in the left figure. A different contrast in PME can be observed in the GB area. The proximity histogram of the PME profile by defining an isosurface using home-coded software EPOSA[119] shows that the PME value drops to about 20% in the GB plane (can be found in the original publication[116]), indicating the collapse of MVB there. As we mentioned above, a large optical dielectric constant and a high Born effective charge are intrinsic properties of MVB compounds due to the large degree of delocalization and polarization of *p*-electrons.[27,81] According to the Lyddane–Sachs–Teller relation,[120] a large static dielectric constant can also be obtained, leading to a strong dielectric screening effect.[121] Thus, the collapse of MVB inevitably decreases the static dielectric constant and weakens the dielectric screening, which is another factor that increases the GB potential barrier height, as sketched in the inset of Figure 4f.[122] In contrast to the high-angle GB, the collapse of MVB only occurs within the dislocation cores at the low-angle GB, while charge carriers can still pass through the areas between dislocation cores. This leads to a much weaker scattering strength at the dislocations for charge carriers, explaining the observations of attractive electrical properties in dislocation-rich MVB thermoelectric materials such as $Bi_{0.5}Sb_{1.5}Te_3$,[123] PbTe,[124] and PbSe.[17]

5. Conclusions and Outlook

This review article has tried to summarize the indispensable role of APT in understanding the phase-change mechanism and designing high-performance thermoelectric materials. We briefly introduced the working principle of the APT technique, which is based on field-induced ionization and evaporation accompanied by breaking chemical bonds. An abnormal bond-rupture behavior with a large PME value is observed for a number of chalcogenides. Interestingly, these chalcogenides can also be used as prototypical phase-change and thermoelectric materials. A unique bonding mechanism, named metavalent bonding, is responsible for these superior properties. The high PME value measured by APT is considered a hallmark of metavalent bonding and, thus, could also be an indicator of promising phase-change and thermoelectric materials. In particular, APT could be employed to determine crystalline nuclei in an amorphous matrix, due to the accompanying changes of PME. We also exemplified the strong capability of APT in characterizing lattice defects, which helps to reveal the switching mechanism of interfacial PCMs as well as the role of defects in determining the thermoelectric properties. Owing to the high spatial resolution of APT and the correlations between bond breaking and chemical bonding mechanisms, APT can also resolve the local structural and chemical bonding transitions at defects. This promotes a deep understanding of the bonding–structure–property relationships, which is of fundamental significance for the rational design of functional materials. Besides PCMs and thermoelectrics, MVB has been shown important in other fields such as halide perovskites[125] and far-infrared transparent conductors.[126] The unique ability of APT to identify metavalent bonding can help to better understand the application properties of these materials from a chemical bonding perspective. Furthermore, the spatial resolution of APT provides unique possibilities to study the impact of local bonding changes on material properties.[116]

Acknowledgements

This work was supported by the German Research Foundation DFG within project SFB 917 (Nanoswitches).

Open Access funding enabled and organized by Projekt DEAL.

Conflict of Interest

The authors declare no conflict of interest.

Keywords

atom probe tomography, chalcogenides, metavalent bonding, phase-change data storage, thermoelectric

Received: June 5, 2023
Revised: July 9, 2023
Published online: July 21, 2023

[1] M. Wuttig, N. Yamada, *Nat. Mater.* **2007**, *6*, 824.
[2] S. Raoux, F. Xiong, M. Wuttig, E. Pop, *MRS Bull.* **2014**, *39*, 703.
[3] D. Lencer, M. Salinga, B. Grabowski, T. Hickel, J. Neugebauer, M. Wuttig, *Nat. Mater.* **2008**, *7*, 972.
[4] G. J. Snyder, E. S. Toberer, *Nat. Mater.* **2008**, *7*, 105.
[5] X.-L. Shi, J. Zou, Z.-G. Chen, *Chem. Rev.* **2020**, *120*, 7399.
[6] T. Zhu, Y. Liu, C. Fu, J. P. Heremans, G. J. Snyder, X. Zhao, *Adv. Mater.* **2017**, *29*, 1605884.
[7] M. Wuttig, *Nat. Mater.* **2005**, *4*, 265.
[8] M. Wuttig, H. Bhaskaran, T. Taubner, *Nat. Photonics* **2017**, *11*, 465.
[9] J. He, T. M. Tritt, *Science* **2017**, *357*, eaak9997.
[10] L. E. Bell, *Science* **2008**, *321*, 1457.
[11] Y. Yu, M. Cagnoni, O. Cojocaru-Mirédin, M. Wuttig, *Adv. Funct. Mater.* **2020**, *30*, 1904862.
[12] M. Hong, M. Li, Y. Wang, X.-L. Shi, Z.-G. Chen, *Adv. Mater.* **2023**, *35*, 2208272.
[13] H. Goldsmid, *Materials* **2014**, *7*, 2577.
[14] B. J. Kooi, M. Wuttig, *Adv. Mater.* **2020**, *32*, 1908302.
[15] M. Wuttig, D. Lusebrink, D. Wamwangi, W. Welnic, M. Gillessen, R. Dronskowski, *Nat. Mater.* **2007**, *6*, 122.
[16] X. Zhang, J. Li, X. Wang, Z. Chen, J. Mao, Y. Chen, Y. Pei, *J. Am. Chem. Soc.* **2018**, *140*, 15883.
[17] L. Xu, Y. Xiao, S. Wang, B. Cui, D. Wu, X. Ding, L. D. Zhao, *Nat. Commun.* **2022**, *13*, 6449.
[18] L. Abdellaoui, Z. Chen, Y. Yu, T. Luo, R. Hanus, T. Schwarz, R. Bueno Villoro, O. Cojocaru-Mirédin, G. J. Snyder, D. Raabe, Y. Pei, C. Scheu, S. Zhang, *Adv. Funct. Mater.* **2021**, *31*, 2101214.
[19] R. Xu, Z. Chen, Q. Li, X. Yang, H. Wan, M. Kong, W. Bai, N. Zhu, R. Wang, J. Song, Z. Li, C. Xiao, B. Ge, *Research* **2023**, *6*, 0123.
[20] P. Xu, W. Zhao, X. Liu, B. Jia, J. He, L. Fu, B. Xu, *Adv. Mater.* **2022**, *34*, 2202949.

[21] Z. Wang, L. Ding, L. Liu, Z. Tan, H. Pan, P. Jiang, W. Wu, Y. Yu, *Scr. Mater.* **2023**, *228*, 115315.
[22] C. Zhang, X. Geng, B. Chen, J. Li, A. Meledin, L. Hu, F. Liu, J. Shi, J. Mayer, M. Wuttig, O. Cojocaru-Miredin, Y. Yu, *Small* **2021**, *17*, 2104067.
[23] C. Zhang, G. Yan, Y. Wang, X. Wu, L. Hu, F. Liu, W. Ao, O. Cojocaru-Mirédin, M. Wuttig, G. J. Snyder, Y. Yu, *Adv. Energy Mater.* **2023**, *13*, 2203361.
[24] R. Shu, Z. Han, A. Elsukova, Y. Zhu, P. Qin, F. Jiang, J. Lu, P. O. A. Persson, J. Palisaitis, A. le Febvrier, W. Zhang, O. Cojocaru-Miredin, Y. Yu, P. Eklund, W. Liu, *Adv. Sci.* **2022**, *9*, 2202594.
[25] N. Mingo, D. Hauser, N. P. Kobayashi, M. Plissonnier, A. Shakouri, *Nano Lett.* **2009**, *9*, 711.
[26] S. Liu, Y. Yu, D. Wu, X. Xu, X. Chao, Z. Yang, J. He, *Small* **2021**, *17*, 2104496.
[27] M. Wuttig, V. L. Deringer, X. Gonze, C. Bichara, J. Y. Raty, *Adv. Mater.* **2018**, *30*, 1803777.
[28] J. Y. Raty, M. Schumacher, P. Golub, V. L. Deringer, C. Gatti, M. Wuttig, *Adv. Mater.* **2019**, *31*, 1806280.
[29] R. Arora, U. V. Waghmare, C. N. R. Rao, *Adv. Mater.* **2023**, *35*, 2208724.
[30] M. Wuttig, C.-F. Schön, J. Lötfering, P. Golub, C. Gatti, J.-Y. Raty, *Adv. Mater.* **2022**, *35*, 2208485.
[31] G. N. Lewis, *J. Am. Chem. Soc.* **1916**, *38*, 762.
[32] J. Hempelmann, P. C. Müller, C. Ertural, R. Dronskowski, *Angew. Chem., Int. Ed.* **2022**, *61*, 202115778.
[33] V. L. Deringer, W. Zhang, M. Lumeij, S. Maintz, M. Wuttig, R. Mazzarello, R. Dronskowski, *Angew. Chem.* **2014**, *53*, 10817.
[34] K. Shportko, S. Kremers, M. Woda, D. Lencer, J. Robertson, M. Wuttig, *Nat. Mater.* **2008**, *7*, 653.
[35] M. Wuttig, *Phys. Status Solidi B* **2009**, *246*, 1820.
[36] M. Wuttig, *Phys. Status Solidi B* **2012**, *249*, 1843.
[37] L. Guarneri, S. Jakobs, A. von Hoegen, S. Maier, M. Xu, M. Zhu, S. Wahl, C. Teichrib, Y. Zhou, O. Cojocaru-Miredin, M. Raghuwanshi, C. F. Schon, M. Drogeler, C. Stampfer, R. Lobo, A. Piarristeguy, A. Pradel, J. Y. Raty, M. Wuttig, *Adv. Mater.* **2021**, *33*, 2102356.
[38] C.-F. Schön, S. van Bergerem, C. Mattes, A. Yadav, M. Grohe, L. Kobbelt, M. Wuttig, *Sci. Adv.* **2022**, *8*, eade0828.
[39] D. Sarkar, S. Roychowdhury, R. Arora, T. Ghosh, A. Vasdev, B. Joseph, G. Sheet, U. V. Waghmare, K. Biswas, *Angew. Chem., Int. Ed. Engl.* **2021**, *60*, 10350.
[40] M. Cagnoni, D. Fuhren, M. Wuttig, *Adv. Mater.* **2018**, *30*, 1801787.
[41] J.-Y. Raty, M. Wuttig, *J. Phys. D: Appl. Phys.* **2020**, *53*, 234002.
[42] S. Maier, S. Steinberg, Y. Cheng, C. F. Schon, M. Schumacher, R. Mazzarello, P. Golub, R. Nelson, O. Cojocaru-Miredin, J. Y. Raty, M. Wuttig, *Adv. Mater.* **2020**, *32*, 2005533.
[43] Y. Cheng, O. Cojocaru-Miredin, J. Keutgen, Y. Yu, M. Kupers, M. Schumacher, P. Golub, J. Y. Raty, R. Dronskowski, M. Wuttig, *Adv. Mater.* **2019**, *31*, 1904316.
[44] Y. Cheng, S. Wahl, M. Wuttig, *Phys. Status Solidi RRL* **2020**, *15*, 2000482.
[45] M. Dutta, T. Ghosh, K. Biswas, *APL Mater.* **2020**, *8*, 040910.
[46] S. Lee, K. Esfarjani, T. Luo, J. Zhou, Z. Tian, G. Chen, *Nat. Commun.* **2014**, *5*, 3525.
[47] T. Matsunaga, N. Yamada, R. Kojima, S. Shamoto, M. Sato, H. Tanida, T. Uruga, S. Kohara, M. Takata, P. Zalden, G. Bruns, I. Sergueev, H. C. Wille, R. P. Hermann, M. Wuttig, *Adv. Funct. Mater.* **2011**, *21*, 2232.
[48] C. Rodenkirchen, M. Cagnoni, S. Jakobs, Y. Cheng, J. Keutgen, Y. Yu, M. Wuttig, O. Cojocaru-Mirédin, *Adv. Funct. Mater.* **2020**, *30*, 1910039.
[49] R. K. Vankayala, T. W. Lan, P. Parajuli, F. Liu, R. Rao, S. H. Yu, T. L. Hung, C. H. Lee, S. I. Yano, C. R. Hsing, D. L. Nguyen, C. L. Chen, S. Bhattacharya, K. H. Chen, M. N. Ou, O. Rancu, A. M. Rao, Y. Y. Chen, *Adv. Sci.* **2020**, *7*, 2002494.
[50] A. D. LaLonde, Y. Pei, H. Wang, G. Jeffrey Snyder, *Mater. Today* **2011**, *14*, 526.
[51] D. Wright, *Nature* **1958**, *181*, 834.
[52] C. Liu, Z. Zhang, Y. Peng, F. Li, L. Miao, E. Nishibori, R. Chetty, X. Bai, R. Si, J. Gao, X. Wang, Y. Zhu, N. Wang, H. Wei, T. Mori, *Sci. Adv.* **2023**, *9*, eadh0713.
[53] Y. Jiang, J. Dong, H. L. Zhuang, J. Yu, B. Su, H. Li, J. Pei, F. H. Sun, M. Zhou, H. Hu, J. W. Li, Z. Han, B. P. Zhang, T. Mori, J. F. Li, *Nat. Commun.* **2022**, *13*, 6087.
[54] B. Jiang, W. Wang, S. Liu, Y. Wang, C. Wang, Y. Chen, L. Xie, M. Huang, J. He, *Science* **2022**, *377*, 208.
[55] B. Jiang, Y. Yu, J. Cui, X. Liu, L. Xie, J. Liao, Q. Zhang, Y. Huang, S. Ning, B. Jia, B. Zhu, S. Bai, L. Chen, S. J. Pennycook, J. He, *Science* **2021**, *371*, 830.
[56] Y. Wu, Z. Chen, P. Nan, F. Xiong, S. Lin, X. Zhang, Y. Chen, L. Chen, B. Ge, Y. Pei, *Joule* **2019**, *3*, 1276.
[57] M. Zhu, O. Cojocaru-Miredin, A. M. Mio, J. Keutgen, M. Kupers, Y. Yu, J. Y. Cho, R. Dronskowski, M. Wuttig, *Adv. Mater.* **2018**, *30*, 1706735.
[58] B. Gault, A. Chiaramonti, O. Cojocaru-Mirédin, P. Stender, R. Dubosq, C. Freysoldt, S. K. Makineni, T. Li, M. Moody, J. M. Cairney, *Nat. Rev. Methods Primers* **2021**, *1*, 51.
[59] B. Gault, *Appl. Microsc.* **2016**, *46*, 117.
[60] D. N. Seidman, *Annu. Rev. Mater. Res.* **2007**, *37*, 127.
[61] F. Vurpillot, B. Gault, B. P. Geiser, D. J. Larson, *Ultramicroscopy* **2013**, *132*, 19.
[62] B. Gault, D. Haley, F. de Geuser, M. P. Moody, E. A. Marquis, D. J. Larson, B. P. Geiser, *Ultramicroscopy* **2011**, *111*, 448.
[63] Z. Peng, F. Vurpillot, P. P. Choi, Y. Li, D. Raabe, B. Gault, *Ultramicroscopy* **2018**, *189*, 54.
[64] L. Hu, B. Duan, T. Lyu, N. Lin, C. Zhang, F. Liu, J. Li, M. Wuttig, Y. Yu, *Adv. Funct. Mater.* **2023**, *33*, 2214854.
[65] Y. Liu, X. Zhang, P. Nan, B. Zou, Q. Zhang, Y. Hou, S. Li, Y. Gong, Q. Liu, B. Ge, O. Cojocaru-Mirédin, Y. Yu, Y. Zhang, G. Chen, M. Wuttig, G. Tang, *Adv. Funct. Mater.* **2022**, 2209980.
[66] D. An, J. Wang, J. Zhang, X. Zhai, Z. Kang, W. Fan, J. Yan, Y. Liu, L. Lu, C.-L. Jia, M. Wuttig, O. Cojocaru-Mirédin, S. Chen, W. Wang, G. J. Snyder, Y. Yu, *Energy Environ. Sci.* **2021**, *14*, 5469.
[67] O. Cojocaru-Mirédin, M. Raghuwanshi, R. Wuerz, S. Sadewasser, *Adv. Funct. Mater.* **2021**, *31*, 2103119.
[68] M. Raghuwanshi, R. Wuerz, O. Cojocaru-Mirédin, *Adv. Funct. Mater.* **2020**, *30*, 2001046.
[69] M. Raghuwanshi, M. Chugh, G. Sozzi, A. Kanevce, T. D. Kühne, H. Mirhosseini, R. Wuerz, O. Cojocaru-Mirédin, *Adv. Mater.* **2022**, *34*, 2203954.
[70] O. Cojocaru-Mirédin, J. Schmieg, M. Müller, A. Weber, E. Ivers-Tiffée, D. Gerthsen, *J. Power Sources* **2022**, *539*, 231417.
[71] Y. Yu, C. Zhou, S. Zhang, M. Zhu, M. Wuttig, C. Scheu, D. Raabe, G. J. Snyder, B. Gault, O. Cojocaru-Mirédin, *Mater. Today* **2020**, *32*, 260.
[72] Y. Wu, P. Qiu, Y. Yu, Y. Xiong, T. Deng, O. Cojocaru-Mirédin, M. Wuttig, X. Shi, L. Chen, *J. Mater.* **2022**, *8*, 1095.
[73] Y. Yu, C. Zhou, X. Zhang, L. Abdellaoui, C. Doberstein, B. Berkels, B. Ge, G. Qiao, C. Scheu, M. Wuttig, O. Cojocaru-Mirédin, S. Zhang, *Nano Energy* **2022**, *101*, 107576.
[74] J. P. Male, L. Abdellaoui, Y. Yu, S. Zhang, N. Pieczulewski, O. Cojocaru-Mirédin, C. Scheu, G. J. Snyder, *Adv. Funct. Mater.* **2021**, *31*, 2108006.
[75] Y. Yu, S. Zhang, A. M. Mio, B. Gault, A. Sheskin, C. Scheu, D. Raabe, F. Zu, M. Wuttig, Y. Amouyal, O. Cojocaru-Miredin, *ACS Appl. Mater. Interfaces* **2018**, *10*, 3609.

[76] C. Zhou, Y. Yu, Y. L. Lee, B. Ge, W. Lu, O. Cojocaru-Miredin, J. Im, S. P. Cho, M. Wuttig, Z. Shi, I. Chung, *J. Am. Chem. Soc.* **2020**, *142*, 15172.
[77] B. Ge, C. Li, W. Lu, H. Ye, R. Li, W. He, Z. Wei, Z. Shi, D. Kim, C. Zhou, M. Zhu, M. Wuttig, Y. Yu, *Adv. Energy Mater.* **2023**, 2300965.
[78] L. Pauling, in *The Nature of The Chemical Bond*, Vol. *260*, Cornell University Press, Ithaca, NY **1960**.
[79] A. Otero-de-la-Roza, E. R. Johnson, V. Luaña, *Comput. Phys. Commun.* **2014**, *185*, 1007.
[80] R. F. W. Bader, M. E. Stephens, *J. Am. Chem. Soc.* **1975**, *97*, 7391.
[81] Y. Yu, C. Zhou, T. Ghosh, C. F. Schon, Y. Zhou, S. Wahl, M. Raghuwanshi, P. Kerres, C. Bellin, A. Shukla, O. Cojocaru-Miredin, M. Wuttig, *Adv. Mater.* **2023**, *35*, 2300893.
[82] K. Thompson, D. Lawrence, D. J. Larson, J. D. Olson, T. F. Kelly, B. Gorman, *Ultramicroscopy* **2007**, *107*, 131.
[83] A. Vella, *Ultramicroscopy* **2013**, *132*, 5.
[84] T. T. Tsong, *Surf. Sci.* **1979**, *85*, 1.
[85] W. Zhang, R. Mazzarello, M. Wuttig, E. Ma, *Nat. Rev. Mater.* **2019**.
[86] R. Zallen, *J. Non-Cryst. Solids* **1985**, *75*, 3.
[87] A. V. Kolobov, P. Fons, A. I. Frenkel, A. L. Ankudinov, J. Tominaga, T. Uruga, *Nat. Mater.* **2004**, *3*, 703.
[88] C. Persch, M. J. Muller, A. Yadav, J. Pries, N. Honne, P. Kerres, S. Wei, H. Tanaka, P. Fantini, E. Varesi, F. Pellizzer, M. Wuttig, *Nat. Commun.* **2021**, *12*, 4978.
[89] S. Sun, L. Zhu, W. Zhang, *Phys. Status Solidi RRL* **2022**, *16*, 2100626.
[90] R. E. Simpson, P. Fons, A. V. Kolobov, T. Fukaya, M. Krbal, T. Yagi, J. Tominaga, *Nat. Nanotechnol.* **2011**, *6*, 501.
[91] X. Yu, J. Robertson, *Sci. Rep.* **2016**, *6*, 37325.
[92] O. Cojocaru-Miredin, H. Hollermann, A. M. Mio, A. Y. Wang, M. Wuttig, *J. Phys. Condens. Matter.* **2019**, *31*, 204002.
[93] J. Momand, R. Wang, J. E. Boschker, M. A. Verheijen, R. Calarco, B. J. Kooi, *Nanoscale* **2017**, *9*, 8774.
[94] X. Zhang, J. Shen, S. Lin, J. Li, Z. Chen, W. Li, Y. Pei, *J. Mater.* **2016**, *2*, 331.
[95] Y. Zhu, L. Hu, S. Zhan, T. Ina, X. Gao, T. Hong, L.-D. Zhao, *Energy Environ. Sci.* **2022**, *15*, 3958.
[96] Z. Bu, X. Zhang, B. Shan, J. Tang, H. Liu, Z. Chen, S. Lin, W. Li, Y. Pei, *Sci. Adv.* **2021**, *7*, eabf2738.
[97] Z. Wang, H. Wu, B. Zhang, L. Dai, Y. Huo, Y. Huang, G. Han, X. Lu, X. Zhou, G. Wang, *Adv. Funct. Mater.* **2022**, *32*, 2111238.
[98] M. Yan, H. Geng, P. Jiang, X. Bao, *J. Energy Chem.* **2020**, *45*, 83.
[99] Z. Huang, S. A. Miller, B. Ge, M. Yan, S. Anand, T. Wu, P. Nan, Y. Zhu, W. Zhuang, G. J. Snyder, P. Jiang, X. Bao, *Angew. Chem., Int. Ed. Engl.* **2017**, *56*, 14113.
[100] M. Yan, X. Tan, Z. Huang, G. Liu, P. Jiang, X. Bao, *J. Mater. Chem. A* **2018**, *6*, 8215.
[101] S. Roychowdhury, T. Ghosh, R. Arora, U. V. Waghmare, K. Biswas, *Angew. Chem., Int. Ed. Engl.* **2018**, *57*, 15167.
[102] B. Duan, Y. Zhang, Q. Yang, Y. Li, J. Cheng, C. Zhang, J. Li, F. Liu, L. Hu, *Adv. Energy Sustain. Res.* **2022**, *3*.
[103] X. Li, Z. Liang, J. Li, F. Cheng, J. He, C. Zhang, J. Li, F. Liu, T. Lyu, B. Ge, L. Hu, *Nano Energy* **2022**, *100*, 107434.
[104] J.-D. Musah, A. M. Ilyas, S. Venkatesh, S. Mensah, S. Kwofie, V. A. L. Roy, C.-M. L. Wu, *Nano Res. Energy* **2022**, *1*, e9120034.
[105] L. D. Zhao, S. H. Lo, Y. Zhang, H. Sun, G. Tan, C. Uher, C. Wolverton, V. P. Dravid, M. G. Kanatzidis, *Nature* **2014**, *508*, 373.
[106] Z.-G. Chen, X. Shi, L.-D. Zhao, J. Zou, *Prog. Mater. Sci.* **2018**, *97*, 283.
[107] L.-D. Zhao, C. Chang, G. Tan, M. G. Kanatzidis, *Energy Environ. Sci.* **2016**, *9*, 3044.
[108] Y. K. Lee, Z. Luo, S. P. Cho, M. G. Kanatzidis, I. Chung, *Joule* **2019**, *3*, 719.
[109] C. Zhou, Y. K. Lee, Y. Yu, S. Byun, Z. Z. Luo, H. Lee, B. Ge, Y. L. Lee, X. Chen, J. Y. Lee, O. Cojocaru-Miredin, H. Chang, J. Im, S. P. Cho, M. Wuttig, V. P. Dravid, M. G. Kanatzidis, I. Chung, *Nat. Mater.* **2021**, *20*, 1378.
[110] J. J. Kuo, S. D. Kang, K. Imasato, H. Tamaki, S. Ohno, T. Kanno, G. J. Snyder, *Energy Environ. Sci.* **2018**, *11*, 429.
[111] T. Luo, J. J. Kuo, K. J. Griffith, K. Imasato, O. Cojocaru-Mirédin, M. Wuttig, B. Gault, Y. Yu, G. J. Snyder, *Adv. Funct. Mater.* **2021**, *31*, 2100258.
[112] Q. Qiu, Y. Liu, K. Xia, T. Fang, J. Yu, X. Zhao, T. Zhu, *Adv. Energy Mater.* **2019**, *9*, 1803447.
[113] Y. Wu, F. Liu, Q. Zhang, T. Zhu, K. Xia, X. Zhao, *J. Mater. Chem. A* **2020**, *8*, 8455.
[114] J. J. Kuo, Y. Yu, S. D. Kang, O. Cojocaru-Miredin, M. Wuttig, G. J. Snyder, *Adv. Mater. Interfaces* **2019**, *6*, 1900429.
[115] H. Shang, Z. Liang, C. Xu, J. Mao, H. Gu, F. Ding, Z. Ren, *Research* **2020**, *2020*, 1219461.
[116] R. Wu, Y. Yu, S. Jia, C. Zhou, O. Cojocaru-Miredin, M. Wuttig, *Nat. Commun.* **2023**, *14*, 719.
[117] C. Hu, K. Xia, C. Fu, X. Zhao, T. Zhu, *Energy Environ. Sci.* **2022**, *15*, 1406.
[118] J. Y. W. Seto, *J. Appl. Phys.* **1975**, *46*, 5247.
[119] J. Keutgen, A. J. London, O. Cojocaru-Miredin, *Microsc. Microanal.* **2020**, *27*, 28.
[120] R. H. Lyddane, R. Sachs, E. Teller, *Phys. Rev.* **1941**, *59*, 673.
[121] R. Su, Z. Xu, J. Wu, D. Luo, Q. Hu, W. Yang, X. Yang, R. Zhang, H. Yu, T. P. Russell, Q. Gong, W. Zhang, R. Zhu, *Nat. Commun.* **2021**, *12*, 2479.
[122] Y. Yu, M. Wuttig, *Nano Res. Energy* **2023**, *2*, 9120057.
[123] S. I. Kim, K. H. Lee, H. A. Mun, H. S. Kim, S. W. Hwang, J. W. Roh, D. J. Yang, W. H. Shin, X. S. Li, Y. H. Lee, *Science* **2015**, *348*, 109.
[124] Z. Chen, Z. Jian, W. Li, Y. Chang, B. Ge, R. Hanus, J. Yang, Y. Chen, M. Huang, G. J. Snyder, Y. Pei, *Adv. Mater.* **2017**, *29*, 1606768.
[125] M. Wuttig, C. F. Schön, M. Schumacher, J. Robertson, P. Golub, E. Bousquet, C. Gatti, J. Y. Raty, *Adv. Funct. Mater.* **2021**, *32*, 2110166.
[126] C. Hu, Z. Zhou, X. Zhang, K. Guo, C. Cui, Y. Li, Z. Gu, W. Zhang, L. Shen, J. Zhu, *Light Sci. Appl.* **2023**, *12*, 98.

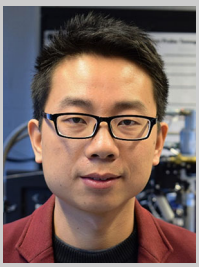

Yuan Yu received his bachelor and Ph.D. degrees in materials science and engineering from Hefei University of Technology in 2008 and 2017, respectively. He then joined Prof. Matthias Wuttig's group as a postdoctoral researcher at RWTH Aachen University in 2018. Since 2022, he leads a group as principal investigator at RWTH Aachen University. He has published about 70 papers in prestigious journals with a H-index of 26. His primary scientific interests include the design and characterization of thermoelectric and phase-change materials through metavalent bonding and atom probe tomography. He is also interested in the structure–property relationship of materials using correlative microscopy.

Oana Cojocaru-Mirédin received her Ph.D. degree in physics in 2009 from the University of Rouen. Afterward, she worked as a postdoc till 2012 at Max-Planck-Institut für Eisenforschung GmbH. By winning the "NanoMatFutur" organized by BMBF in Germany, she became in 2013 the head of "Interface Design in Solar Cells" group. In 2015, she moved to RWTH Aachen University where she led the "Nanocharacterization of Advanced Functional Materials" group. Since 2022, she is a professor at the University of Freiburg and leads the chair "Cross-scale Material Characterization". Her research interests include the characterization and processing of compound semiconductors for energy applications.

Matthias Wuttig received his Ph.D. in physics in 1988 from RWTH Aachen/ Forschungszentrum Jülich. He was a visiting professor at several institutions including Lawrence Berkeley Laboratory, CINaM (Marseille), Stanford University, Hangzhou University, IBM Almaden, Bell Labs, DSI in Singapore, and the Chinese Academy of Sciences in Shanghai. In 1997, he was appointed full professor at RWTH Aachen. Since 2011, he heads a collaborative research center on resistively switching chalcogenides (SFB 917), funded by the DFG. He won an ERC Advanced Grant in 2013 and is a Fellow of the MRS since 2019.